

Real-time scattering compensation for time-of-flight camera

James Mure-Dubois and Heinz Hügli

University of Neuchâtel
Institute of Microtechnology, 2000 Neuchâtel, Switzerland

Abstract. 3D images from time-of-flight cameras may suffer from false depth readings caused by light scattering. In order to reduce such scattering artifacts, a scattering compensation procedure is proposed. First, scattering is analysed and expressed as a linear transform of a complex image. Then, a simple scattering model is formulated. Assuming a space invariant point spread function as a model for the scattering leads to a solution in a form of a deconvolution scheme whose computational feasibility and practical applicability are further discussed in this paper.

1 Introduction

Recent time-of-flight (TOF) cameras acquire 3D information about scenes in real-time, with high depth resolution, two properties which ensure that such cameras will soon be used in many demanding applications such as automotive, quality control, biometrics, surveillance, etc. TOF cameras rely on active illumination, and deliver range data by measuring the time needed for light to travel from the camera light source to the scene and back to the camera. However, depth measurement may be affected by secondary reflections, namely by reflections between the lens and imager, designated thereafter by scattering. In situations where a wide range of depths is imaged, the large signal range can make scattering from close objects come in competition with the primary signal from far objects, causing artifacts in the depth measurements. This degradation of the depth image is a significant penalty in many applications, especially when background subtraction methods are employed [1].

This paper provides an analysis of the scattering that affects TOF cameras and proposes means to reduce its effects by an image processing compensation procedure that applies to the affected image. In section 2, we describe the scattering effect and propose an algebraic formulation of its mechanism: scattering is interpreted as a linear additive contribution to a complex signal. Then, a real valued point spread-function (PSF) is used to describe the perturbation in a simple way. In section 3, we present scattering compensation methods. Based on the PSF approach, scattering compensation is expressed as a blind deconvolution problem for a complex signal. Avoiding the superior complexity of blind deconvolution, we use an empirical estimate of the PSF and straightforward deconvolution. Section 4 proposes a scattering model suited for real-time compensation, introduces



empirical estimation of its PSF, and presents experimental results showing the ability of the proposed method to reduce depth artifacts caused by scattering. Finally, section 5 summarizes our contribution to scattering compensation and lists further possible developments to improve its performance.

2 Scattering in time-of-flight cameras

2.1 Operation of a time-of-flight camera

Time-of-flight cameras involve active illumination, and deliver range (or depth) data by measuring the time needed for a light signal to travel from the camera light source to the scene and back to the camera sensor, as illustrated in figure 1. Present cameras ([2],[3]) are based on the continuous emission of a periodic signal. The frequency of modulation f of this signal is typically 20MHz. The periodic signal $S(\mathbf{i})$ received at each pixel (\mathbf{i}) of the camera sensor is described by its amplitude $A(\mathbf{i})$ and its phase $\varphi(\mathbf{i})$. The range r is directly proportional to the phase. With c as the speed of light, we have :

$$S(\mathbf{i}) = A(\mathbf{i}) \cdot e^{j\varphi(\mathbf{i})} \quad r(\mathbf{i}) = \frac{c}{4\pi f} \cdot \varphi(\mathbf{i}) \quad (1)$$

2.2 Range measurement degraded by scattering

When an ideal signal $S(\mathbf{i})$ is affected by a parasitic additive contribution $\Delta S(\mathbf{i})$ of different phase, produced for example by light scattering, the phase of the new complex signal $S + \Delta S$ differs from the original phase in a proportion that increases with the ratio $\Delta A/A$ of the respective signal amplitudes. The amplitude A influences therefore the reliability of the depth measurement. The major parameters affecting this quantity are the range r to the imaged object, the angle θ of light incidence on the surface and the object albedo ρ :

$$A \propto \frac{\rho \cdot \cos(\theta)}{r^2} \quad (2)$$

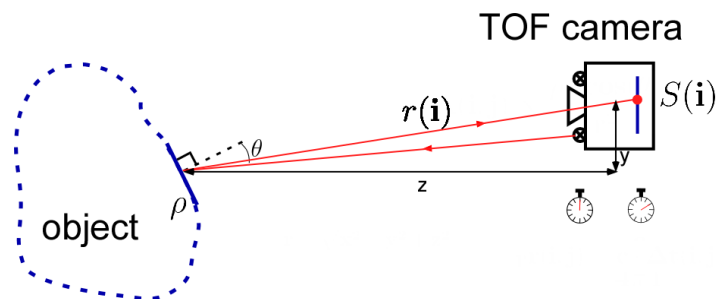


Fig. 1: Time-of-flight camera - Principle of operation

In a practical situation, the spread of possible values for r , θ and ρ results in a very high amplitude dynamic range that the camera must handle. In particular, when the spread of depths is wide, the $1/r^2$ behaviour is critical, since it results in very strong amplitude level differences.

Such a situation is illustrated in figure 2. The scene imaged is an office room (2a). A reference range image is taken when the room is empty (2b). A second range image is acquired in the same conditions, except for the presence of a close person in the field of view (2c). Comparison of both range images shows how the depth of the unchanged background is affected by light from the close person. The range difference between the two acquisitions was reported in fig. (2d). In this example, the measured range for the unchanged background decreases in presence of the person by values ranging from 100 to 400 mm.

2.3 Linear scattering model

Scattering artifacts are caused by multiple internal reflections occurring inside the camera device [4], as illustrated in figure 3 by a simple example with three pixels. Figure 4 shows the related complex signals $S(1)$, $S(2)$, and $S(3)$, first in absence of scattering (4a), then with scattering present (4b). This example shows how parasitic reflections from a strong signal source $S(1)$ can come in competition with the direct signal from far objects $S(2)$ and $S(3)$. Under the assumption of a linear process, we can describe this coupling through coefficients

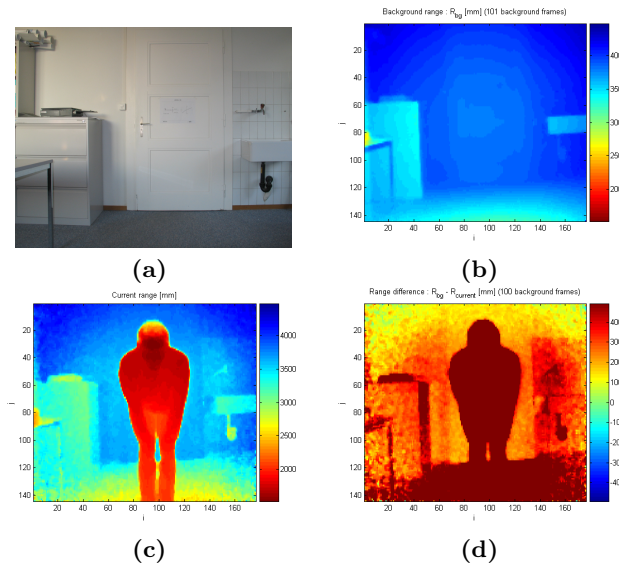


Fig. 2: Illustration of depth artifacts - (a) Color image - (b) Background range image - (c) Range image with foreground. - (d) Range image difference

arranged in a 3x3 matrix \mathfrak{h} , and the measured signals S_{meas} are then given by the expression :

$$S_{meas}(i) = \sum_{m=1}^3 \mathfrak{h}(i, m) \cdot S(m) \quad i = 1, 2, 3 \quad (3)$$

where the superposition of different signals is computed as an addition in the complex plane.

Since, in TOF imaging, far objects have a low amplitude (eq. 2), they are most affected by the scattering phenomenon. This is verified for signals $S(2)$ and $S(3)$ in our example. Moreover, this model explains why depth artifacts are often not necessarily associated with a significant change in the amplitude measured for the affected pixels. In figure 4, the phase difference between $S(1)$ and $S(3)$ is such that the perturbation by $S(1)$ on $S(3)$ creates a large range artifact: $\varphi_{meas}(3) \neq \varphi(3)$, but a negligible amplitude change: $A_{meas}(3) \approx A(3)$.

Extending this model to all pixels of an image $S(i, j)$, we write :

$$S_{meas}(i, j) = \sum_m \sum_n \mathfrak{h}(i, j, m, n) \cdot S(m, n) \quad (4)$$

where the four-dimensional tensor $\mathfrak{h}(i, j, m, n)$ contains real-valued, linear coupling coefficients ($\mathfrak{h}(i, j, m, n) \in \mathbb{R} \forall (i, j, m, n)$, $\frac{\partial}{\partial S} \mathfrak{h} = 0$). To discuss only scattering, we can formally split the measured signal into an ideal signal \mathbf{S} and a scattering signal \mathbf{S}_{scat}

$$S_{meas}(i, j) = S(i, j) + S_{scat}(i, j) \quad (5)$$

From our linear assumption (eq. 4), we can express \mathbf{S}_{scat} through a linear "scattering-only" tensor $\Delta\mathfrak{h}(i, j, m, n)$ such that :

$$S_{scat}(i, j) = \sum_m \sum_n \Delta\mathfrak{h}(i, j, m, n) \cdot S(m, n) \quad (6)$$

The general solution is complex and we propose a simplification by assuming space invariant scattering.

2.4 Space invariant model

The assumption of space invariant scattering is that the magnitude of the coupling between two pixels depends only on their spatial separation. With this hypothesis, we can rewrite eq. 6 as a convolution operation :

$$S_{scat}(i, j) = \sum_m \sum_n \Delta\mathfrak{h}(i - m, j - n) \cdot S(m, n) = S(i, j) ** \Delta h(i, j) \quad (7)$$

where $**$ denotes the 2D convolution. If we define \mathbf{h}_0 as the neutral element with respect to convolution, we can express equation 5 with a convolution operation :

$$S_{meas}(i, j) = S(i, j) ** (h_0(i, j) + \Delta h(i, j)) = S(i, j) ** h(i, j) \quad (8)$$

where $\mathbf{h} = \mathbf{h}_0 + \Delta\mathbf{h}$ is interpreted as a camera point spread function including scattering coupling.



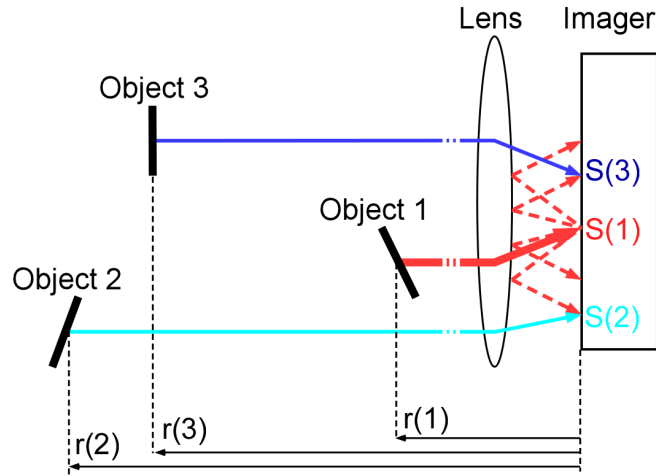


Fig. 3: Light scattering in TOF camera (after [4]).

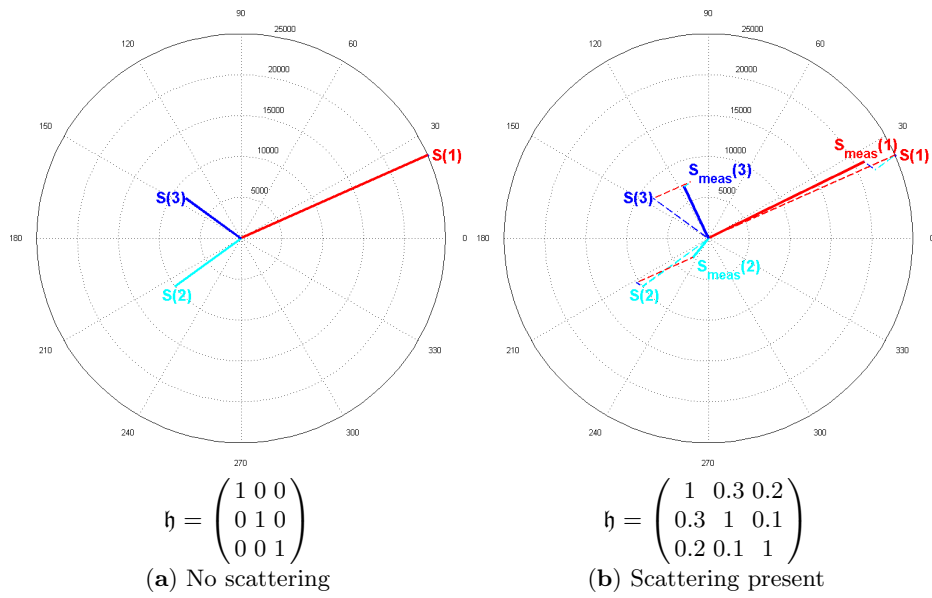


Fig. 4: Example of coupling between three measurement points



3 Scattering compensation

3.1 Goal of scattering compensation

The goal of scattering compensation is to recover \mathbf{S} , based on the signal \mathbf{S}_{meas} returned by the camera. Moreover, to be interesting in a practical application, the complexity of the compensation method used should be low enough to allow for real-time processing. Finally, the practical application we consider (range measurement with time-of-flight camera) puts the emphasis on precise recovery of the phase information Φ , whereas recovery of amplitude \mathbf{A} is considered secondary.

3.2 Deconvolution

With the convolution model expressed in equation 8, recovery of the signal \mathbf{S} from a measurement of \mathbf{S}_{meas} falls into the category of deconvolution problems. More specifically, since the PSF \mathbf{h} is not known *a-priori*, scattering compensation is a *blind deconvolution* problem. Unfortunately, blind deconvolution is an ill-posed problem [5], [6], even for real valued signals. In the case of time-of-flight scattering, the signal for blind deconvolution is complex. Although blind deconvolution algorithm for complex data have been proposed, they are practically limited to few signals sources [7],[8],[9] and, when applied to images, small image size [10]. Moreover, blind deconvolution methods are expected to fail on problems where the difference between degraded and original data is a small amplitude residual.

Since, in the practical application, only the recovery of \mathbf{S} is required, we can avoid the complexity of blind deconvolution by assuming the existence of an inverse filter (deconvolution filter).

Inverse filter for deconvolution In the following discussion, we assume the existence of an inverse filter \mathbf{I} which performs the deconvolution, that is :

$$\mathbf{S} = \mathbf{S}_{meas} ** \mathbf{I} \quad (9)$$

Using again \mathbf{h}_0 , the neutral PSF with respect to convolution, we can write $\mathbf{I} = \mathbf{h}_0 - \Delta\mathbf{I}$ so that eq. 9 takes the form :

$$\mathbf{S} = \mathbf{S}_{meas} - \mathbf{S}_{meas} ** \Delta\mathbf{I} \quad (10)$$

By identification in eq. 5, we have $\mathbf{S}_{scat} = \mathbf{S}_{meas} ** \Delta\mathbf{I}$. Knowledge of $\Delta\mathbf{h}$ or $\Delta\mathbf{I}$ is equivalent, since those two filters are linked through the Fourier transform :

$$\mathbf{I} = \mathbf{h}_0 - \Delta\mathbf{I} = \mathcal{F}^{-1} \{1/\mathcal{F} \{ \mathbf{h}_0 + \Delta\mathbf{h} \} \} \quad (11)$$

However, using eq. 10 is more convenient for scattering compensation, since it involves the measured signal \mathbf{S}_{meas} rather than the original signal \mathbf{S} , which we try to recover. More details on how an appropriate inverse filter $\Delta\mathbf{I}$ can be determined experimentally are given in section 4.



4 Experimentation

4.1 Separable inverse filter

The practical implementation for recovery of \mathbf{S} is based on eq. 10. Aiming for real-time operation, we choose to express our candidate correction operator $\hat{\Delta\mathbf{I}}$ as a weighed sum of separable gaussian kernels of different standard deviation.

$$\hat{\Delta I}(i, j) = \sum_{k=1}^G w(k) \cdot I_h(i, k) \cdot I_v(j, k) \quad (12)$$

where :

- \mathbf{I}_h is a 1D horizontal gaussian kernel ($\in \mathbb{R}$): $I_h(i, k) = \frac{1}{\sqrt{2\pi}\sigma_h(k)} e^{-\frac{i^2}{2\sigma_h^2(k)}}$
- \mathbf{I}_v is a 1D vertical gaussian kernel ($\in \mathbb{R}$): $I_v(j, k) = \frac{1}{\sqrt{2\pi}\sigma_v(k)} e^{-\frac{j^2}{2\sigma_v^2(k)}}$
- $w(k)$ is a scalar ($\in \mathbb{R}$) weight.

The resulting scattering compensation process is illustrated schematically in figure 5. In the next paragraph, we describe an approach to estimate $\Delta\mathbf{I}$ experimentally.

4.2 Estimating the inverse filter

Ideally, $\Delta\mathbf{h}$ should be determined from the response \mathbf{h} of the system when stimulated with a point source. The inverse filter $\Delta\mathbf{I}$ could then be computed from relation 11. Unfortunately, this approach is not practical for two main reasons : no scattering point source exists, and the efficiency of scattering coupling is too low allow a reliable measurement of the impulse response : $\Delta h_{max} < 10^{-5}$.

The approach chosen to overcome this difficulty is to empirically estimate the inverse filter $\Delta\mathbf{I}$ by trial and error by a human expert. A real-time implementation of the scattering compensation method based on eq. 10 was realized, for inverse filters expressed as sums of gaussians, and where the candidate inverse filter $\hat{\Delta\mathbf{I}}$ can be modified by the human expert. During the training, a scene containing only far objects is imaged, and recorded as a background reference. In a second phase, a foreground object is introduced in the field of view, causing scattering. The human expert compares the output of the scattering compensation process with the recorded background. Based on the mismatch in range for background pixels, the description of the inverse filter is adjusted, aiming for reduction of scattering artifacts in the range map. For complexity reasons, the inverse filter description is limited to the sum of a small number of gaussian kernels. Note also that with this method, the computation load is determined by the extent of the kernels.

A typical model is given below. It is specified by three gaussians and their respective weights.

k	σ_h	σ_v	w
1	32	64	0.1000
2	48	48	0.0700
3	64	64	0.1800

 (13)

4.3 Performance

To evaluate the performance of the proposed scattering compensation method, we perform experiments in which a scene is measured without and with a foreground acting as a scattering source. The depth measured when the foreground is absent is considered as ground truth¹. In scenes where the foreground is present, each background pixel is compared to its recorded depth (the foreground object is excluded by depth segmentation). In the example of fig. 2, the average lift on all background pixels is reduced from 33cm to 12cm when scattering compensation is used. This represents a 60% damping in scattering artifacts.

To check the validity of the approach, background lift must be compared for various configurations of camera and scatterer. Therefore, an experiment was performed where the same foreground object was positioned at four different distances from the camera, with three different background textures. Distance to background is the same in all situations : 180cm. Figure 6 summarises the experiments. The average background lift is plotted as a function of the foreground object distance, for the three background situations. Absence of scattering is characterized by a null lift (green curve). Red curves represent the average lift for the raw signals, while the blue curves represent the average lift for signals where scattering compensation was applied. First, we verify that the compensation procedure works well in the limit of low scattering : when the distance between foreground and camera is large, the lift is not noticeable. Note how the green, blue and red curves merge for distances $r > 1100\text{ mm}$. For larger scattering, the raw data always shows more background lift than data with scattering compensation. The improvement varies between 95% and 38% in difficult situations.

We verify that distance between scatterer object and camera is critical for scattering artifacts. We can also note that compensation is more efficient when scattering is small (i.e. for a bright background, or when the scatterer is far away).

5 Conclusions

In this paper, we studied scattering artifacts observed in TOF imaging and introduced an image processing compensation method. Competition between primary signal and scattering was described using the complex representation. Hypotheses of linearity and space invariance were used to develop a model where scattering is expressed by a convolution operation. This model was then used to investigate scattering compensation methods. By restricting the inverse filter to convolution kernels expressed as sums of separable gaussians, we were able to propose a scattering compensation procedure working in real-time. Using only output data from the TOF camera, we built an estimate of the inverse filter, which was then used for scattering compensation. The experimental application

¹ More specifically, background is computed as the average of 100 or more frames of the empty scene.



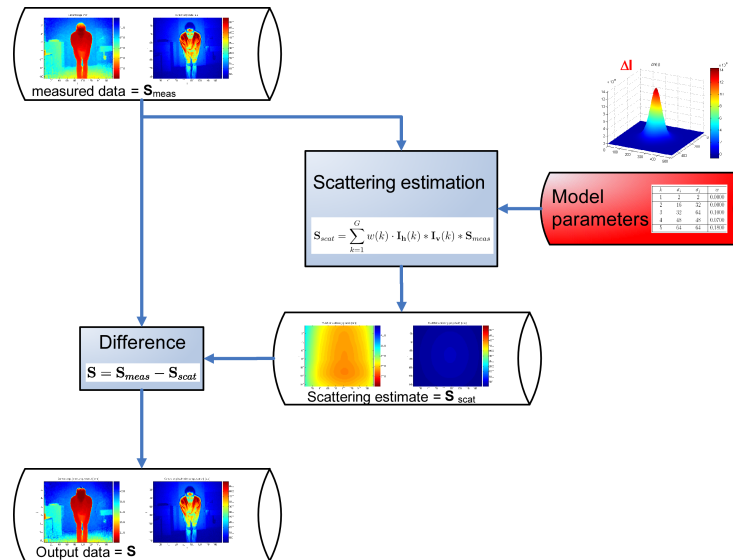


Fig. 5: Scattering compensation - Real time implementation: subtraction of scattering estimate, computed with compensation kernel expressed as a sum of separable gaussians.

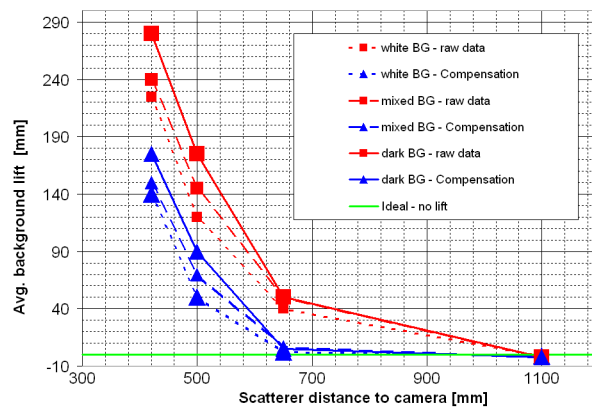
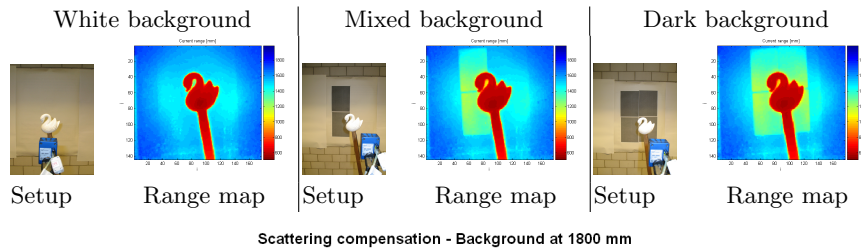


Fig. 6: Scattering compensation experiments

of this procedure resulted in a reduction of scattering (measured from the average background lift) by values ranging from 95% at best to 38% in difficult situations.

For even better compensation results, the proposed approach can be extended in the future. First, the empirical determination of scattering kernel could be improved through automated optimization. Moreover, as results in different test situations suggest that position independence is not fully verified, a more advanced version of scattering model, allowing for instance a variable compensation kernel $\Delta\mathbf{I}$ could be considered.

Acknowledgements

This work was supported by the Swiss Federal Innovation Promotion Agency KTI/CTI (Projet no. 7719.1 ESPP-ES). The authors would like to thank Thierry Zamofing at CSEM SA for the rich discussions on scattering origins and modelling.

References

1. Santrac, N., Friedland, G., Rojas, R.: High Resolution Segmentation with a Time-of-flight 3D-Camera using the Example of a Lecture Scene (September 2006) Technical report, available from: <http://www.inf.fu-berlin.de/inst/ag-ki/eng/index.html>.
2. CSEM: Swissranger (2006) <http://www.swissranger.ch>.
3. Canesta Inc.: Canestavision (2006) <http://www.canesta.com/index.htm>.
4. CSEM: Swissranger SR-3000 manual v1.02 (June 2006) <http://www.swissranger.ch/customer>.
5. Puetter, R.C., Gosnell, T.R., Yahil, A.: Digital Image Reconstruction: Deblurring and Denoising. *Annual Review of Astronomy and Astrophysics* **43** (September 2005) 139–194
6. Ayers, G.R., Dainty, J.C.: Iterative blind deconvolution method and its applications. *Optics Letters* **13** (July 1988) 547–549
7. Cappe, O.: dcv : A set of matlab functions for blind deconvolution of discrete signals (November 1998) Matlab toolbox - Available from: <http://www.tsi.enst.fr/cappe/dcv/index.html>.
8. Taylor, R.M., L., M., Zaghoul, A.I.: Optimal multichannel blind deconvolution for parametrized channels and known source densities (2005) Technical paper - Available from: http://www.mitre.org/work/tech_papers/tech_papers_05/05_0728/.
9. Gautherat, E., G., G.: Parametric estimation in noisy blind deconvolution model : a new estimation procedure (December 2006) Available from: <http://www.crest.fr/pageperso/gauthera/gauthera.htm>.
10. Ghiglia, D.C., Romero, L.A.: Blind deconvolution of two-dimensional complex data (January 1994) Technical report - Available from: <http://www.osti.gov/energycitations/servlets/purl/10127824-8yLcoE/native/>.

